The Influence of Solubilizing Chain Stereochemistry on Small Molecule Photovoltaics

Raghida Bou Zerdan, Nathan T. Shewmon, Yu Zhu, John P. Mudrick, Kyle J. Chesney, Jiangeng Xue, and Ronald K. Castellano**

Three stereochemically pure isomers and two isomeric mixtures of a solution-processable diketopyrrolopyrrole-containing oligothiophene (SMDPPEH) have been used to study the effect of 2-ethylhexyl solubilizing group stereochemistry on the film morphology and bulk heterojunction (BHJ) solar cell characteristics of small molecule organic photovoltaics. The different SMDPPEH stereoisomer compositions exhibit nearly identical optoelectronic properties in the molecularly dissolved state, as well as in amorphous films blended with PCBM. However, for films in which SMDPPEH crystallization is induced by thermal annealing, significant differences in molecular packing between the different stereoisomer formulations are observed. These differences are borne out in photovoltaic device characteristics for which unannealed devices show very similar behavior, while after annealing the *RR*- and *SS*-SMDPPEH enantiomers show blue-shifted peak EQE relative to the SMDPPEH isomer mixtures. Unannealed devices made from the most crystalline stereoisomer, meso *RS*-SMDPPEH, are not completely amorphous, and show improved photocurrent generation as a result. Unlike the other compounds, after thermal annealing the *RS*-SMDPPEH devices show reduced device performance. The results reveal that the chirality of commonly used 2-ethylhexyl solubilizing chains can have a significant effect on the morphology, absorption, and optimum processing conditions of small molecule organic thin films used as photovoltaic device active layers.

1. Introduction

π-Conjugated organic semiconductors remain actively pursued for diverse solid state photonic, electronic, and optoelectronic device applications. Device fabrication involves either vacuum deposition or solution processing of the active materials; while the former offers highly controlled thickness and uniformity as well as readily available multilayer structures, the latter is promising for large scale, low cost, and low temperature production.[1] Dissolution of otherwise aggressively aggregating π-conjugated materials for thin film preparation from solution requires judicious choice of pendent solubilizing groups,[2,3] typically saturated hydrocarbon chains that promote favorable van der Waals interactions with polarizable organic solvents and weaken intermolecular π–π interactions.[3] For applications that mutually rely on good solution processability, closely packed π-surfaces, and appropriate active layer morphology (e.g., field-effect transistors or FETs, photovoltaics, etc.), solubilizing groups emerge as important structural components for study and material/device optimization. Indeed, for both oligomers and polymers, side chain type,[4–13] length,[14–28] branching,[19,22,29–34] placement,[35–39] and stereochemistry[40–49] have independently been shown to influence thin film morphology, charge carrier mobility, and device performance.[50–52]

Among the most popular solubilizing groups in the organic materials community is "2-ethylhexyl" (EtHx),[53–63] and it comes pre-installed on many commercially-available building blocks for π-conjugated oligomer/polymer preparation. Given the substituent's asymmetric carbon atom, mixtures of stereoisomers are formed in syntheses that begin from racemic starting materials. For molecules bearing two or more EtHx side chains, mixtures include enantiomers and diastereomers, although the isomeric complexity is generally ignored. While the stereoirregularity presumably reduces crystallinity and improves solubility,[40] the ramifications for otherwise carefully performed structure-property-function studies involving organic π-systems, particularly small molecules, have only recently come to light.[40] The motivation of the current work is to understand to what extent it is reasonable to ignore the stereochemistry of the EtHx solubilizing group, and the isomeric complexity it creates, for small π-conjugated molecule morphology and bulk heterojunction photovoltaic devices.

R. Bou Zerdan,[+] Y. Zhu, K. J. Chesney,
Prof. R. K. Castellano
Department of Chemistry
P.O. Box 117200
University of Florida
Gainesville, FL, USA
E-mail: castellano@chem.ufl.edu
N. T. Shewmon,[+] J. P. Mudrick, Prof. J. Xue
Department of Materials Science and Engineering
P.O. Box 116400
University of Florida
Gainesville, FL, USA
E-mail: jxue@mse.ufl.edu
[+]R.B.Z. and N.T.S. contributed equally to this work.

DOI: 10.1002/adfm.201401030

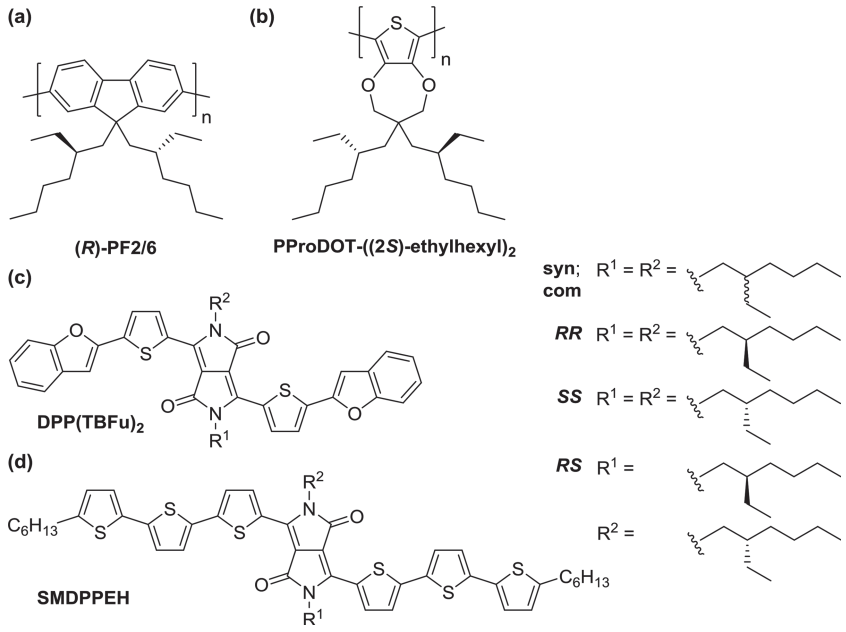

Figure 1. π-Conjugated polymers (a,b) and small molecules (c,d) prepared in stereocontrolled fashion with respect to their 2-ethylhexyl side chains. **SMDPPEH** has been studied in the current work.

For polymeric π-systems, the consequences of stereocontrol with respect to the EtHx side chain have been modestly evaluated. For example, (*R*)-2-ethylhexyl side chains biased the helical backbone conformation of polyfluorene homopolymers **(*R*)-PF2/6** (**Figure 1**a),[64] leading to enhanced chiroptical properties in the solid state. For **PProDOT-((2*S*)-ethylhexyl)$_2$** (Figure 1b), prepared by Reynolds and coworkers,[41] the chiral side chains further encouraged the formation of chiral aggregates in solution. Interestingly, the solid state electronic (i.e., electrochemical potentials, conductivity) and optical (i.e., λ_{max}, optical gap) properties of the enantiomerically pure polymer were essentially identical to **PProDOT-(ethylhexyl)$_2$** (not shown) prepared from racemic EtHx starting materials.[41] One conclusion, although not put forth by the authors, is that the solubilizing chain stereochemical details are washed out in disperse polymer environments with respect to bulk thin film properties.

In contrast, Nguyen and coworkers have recently reported a significant influence of EtHx stereoisomerism on π-conjugated oligomer crystallization behavior and consequently thin film morphology and FET characteristics.[40] Independent characterization of the three stereoisomers (*RR*, *SS*, and *RS*) of **DPP(TBFu)$_2$** (isolated by chiral HPLC separation) (Figure 1c) as well as the as-synthesized material (a roughly statistical mixture of stereoisomers) revealed greater planarity, smaller interplanar (π–π) spacing, red-shifted absorption, and several fold higher hole mobility for the centrosymmetric *RS* isomer versus the *RR*/*SS* isomers and the isomeric mixture.[40] To the best of our knowledge, a comparable analysis in the context of small molecule bulk heterojunction photovoltaics has not been performed.

Reported here are the functional consequences of 2-ethylhexyl stereochemistry on the optical, electrical, morphological, and photovoltaic properties of **SMDPPEH** (Figure 1d), a well-studied[55,65,66] and commercially-available organic semiconductor. The requisite stereoisomers of the material (***RR*-**, ***SS*-**, and ***RS*-SMDPPEH**) have been independently synthesized and then characterized together with as-synthesized (**syn-SMDPPEH**) and commercially-available (**com-SMDPPEH**) samples that are stereoisomeric mixtures. Our results show that side chain stereochemistry and stereoisomeric composition have measurable consequences on the morphology, charge transport characteristics, and photophysical properties of the active layer and the shape of the absorption spectra of the neat materials, but have a limited effect on the overall photovoltaic performance in bulk heterojunction devices.

2. Results and Discussion

2.1. Synthesis

Five different **SMDPPEH** compositions were employed in this study: **com-SMDPPEH** (sublimed, 97% (HPLC), commercially-obtained from Sigma-Aldrich and used without further purification), **syn-SMDPPEH** (prepared from racemic reagents in our laboratory), and the pure stereoisomers (***RR*-**, ***SS*-** and ***RS*-SMDPPEH**) available through stepwise synthesis involving the independently prepared enantiomers of 2-ethylhexyl bromide (3-(bromomethyl)heptane) **1*R*** and **1*S*** (**Scheme 1**). Our approach to **1** recognized that 2-ethylhexanol **2**, a suitable precursor, has been prepared in enantiomerically enriched form through chemical synthesis[41,67] (and more recently via enzymatic reduction of 2-ethylidenehexan-1-ol).[42] We made small adjustments to a synthesis of **2**[67] that began from Evans' chiral oxazolidinone[68] as shown for **1*R*** (Scheme 1). Acylation of (*R*)-4-benzyl-2-oxazolidinone **3*R*** with the in situ generated mixed anhydride derivative of hexanoic acid afforded

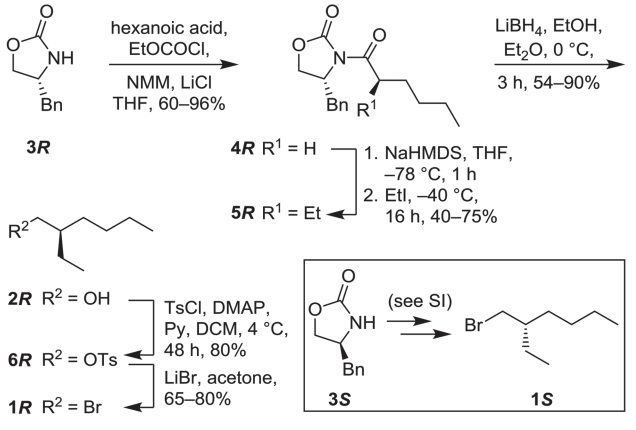

Scheme 1. Synthesis of enantiomerically enriched 2-ethylhexyl bromide **1*R*** and **1*S***.

4*R*.[69] Deprotonation with sodium bis(trimethylsilyl)amide followed by addition of ethyliodide gave **5*R*** (in moderate yield but excellent diastereopurity),[67] and subsequent reduction using lithium borohydride yielded 2-ethylhexanol **2*R***.[67] Spectroscopic and analytical data for **2*R***, including optical rotation, are identical to those reported in the literature (see the Supporting Information for details).[41,42,70] Direct conversion to the bromide proved troublesome under a variety of conditions.[71–73] Replacement of the hydroxyl group with a bromine, *via* the Appel reaction, generated a mixture of 2-ethylhexyl bromide **1*R*** and 1,2-dibromooctane, for example. The desired product was difficult to isolate by column chromatography. Fortunately, conversion of **2*R*** first to the corresponding tosylate **6*R***,[74] followed by treatment with lithium bromide gave **1*R*** cleanly. Preparation of **1*S*** from **3*S*** was performed similarly (see Scheme S2). The high enantiomeric excess of **1*R*** and **1*S*** (>95%) was established by chiral HPLC of subsequent products (vide infra).

Synthesis of the **SMDPPEH** materials then followed the general approach pioneered by Nguyen and coworkers beginning from readily prepared dihydropyrrolo[3,4-*c*]pyrrole-1,4-dione **7** (**Scheme 2**).[75,76] **syn-SMDPPEH**, ***RR*-SMDPPEH**, and ***SS*-SMDPPEH** were prepared using (±)-2-ethylhexyl bromide, **1*R***, and **1*S***, respectively, as *N*-alkylating agents (Schemes S3, S4, and S6). Only the synthesis of ***RS*-SMDPPEH** is shown (Scheme 2) as it required a stepwise *N*-alkylation procedure. Reaction of **1*R*** with a 10-fold excess of **7** generated the monoalkylated product **8*R***, which was further alkylated with **1*S*** to afford **9*RS***. Bromination of the terminal thiophenes of **9*RS*** with *N*-bromosuccinimide (NBS) and subsequent palladium-catalyzed Suzuki coupling with commercially available boronic ester **11** generated ***RS*-SMDPPEH** in amounts suitable for solution-phase and thin film investigation. All five compounds were successfully analyzed by ^{1}H NMR, ^{13}C NMR, HRMS, and elemental analysis. Worth noting, **syn-** and **com-SMDPPEH** showed no evidence by NMR of existing as isomeric mixtures.

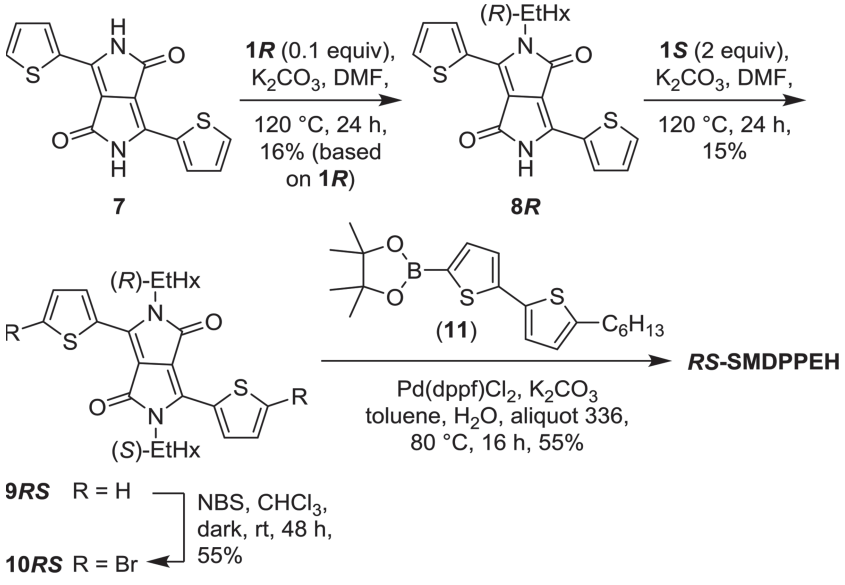

Scheme 2. Synthesis of ***RS*-SMDPPEH**.

2.2. Isomeric Composition

The stereoisomeric purity of ***RR*-**, ***SS*-** and ***RS*-SMDPPEH**, as well as the isomeric composition of **syn-SMDPPEH** and **com-SMDPPEH**, were evaluated by chiral HPLC using the conditions established by Nguyen and coworkers (Figures S1–S3).[40] Analysis of the independently synthesized isomers reveals just one major peak in each case confirming their excellent isomeric purity (~ 97%); the technique also provides the individual isomer retention times (***SS*** = 50 ± 1 min; ***RS*** = 58 ± 1 min; and ***RR*** = 69 ± 1 min). Analogous to the synthesis of **DPP(TBFu)$_2$**,[40] preparation of **SMDPPEH** from (±)-2-ethylhexyl bromide should generate the ***SS*-**, ***RS*-** and ***RR*-** stereoisomers in a statistically predicted 1:2:1 (25%, 50%, 25%) ratio, respectively. Three peaks are indeed detected for **com-SMDPPEH** in a nearly statistical area ratio of 24:48:28. For **syn-SMDPPEH**, the component ratios (Figures S4 and S5) deviate slightly from the commercial material (Figure S6) depending on the synthetic batch and final target purification protocol (e.g., batch #1 (one chromatography column and two recrystallizations): 28:42:30; batch #2 (one chromatography column and one recrystallization): 26:41:33). While it is difficult to say whether the differences are statistically meaningful, the results should give pause to practitioners who assume that oligomer synthesis necessarily provides batch-to-batch reproducibility. The stereoisomeric ratios for π-systems containing two or more EtHx substituents can easily vary depending on synthetic preparation and purification.

2.3. Molecular Properties

The optical properties of the **SMDPPEH** formulations were first evaluated in dilute solution ($CHCl_3$; 2.5×10^{-6} M – 30×10^{-6} M). All five share identical UV-Vis absorption spectra (**Figure 2** and **Table 1**), confirming that the chiral side chain exerts no influence on the intrinsic electronic properties of the chromophores or their solution-phase conformations. Linear Beer-Lambert plots additionally confirmed that no aggregation occurs at the considered concentrations (Figures S7–S16). Three maxima are observable in the UV-visible region. The high energy absorption band (λ = 384 nm) corresponds to a π–π^* transition for both the thiophene and the central diketopyrrolopyrrole (DPP) units,[66,77] while the absorption in the visible region (maxima at 616 and 646 nm) is assigned as an intramolecular charge transfer transition. The extinction coefficients for these materials only vary slightly, and all show expectedly low optical gaps of 1.77 eV consistent with their strong donor-acceptor character (Table 1).[78] Finally, fully consistent with the absorption data, representative **SMDPPEH** compositions have nearly identical electrochemical potentials (based on CV/DPV measurements) in dichloromethane (Table S1 and Figures S17–S19). The HOMO energies (average = –5.36 eV), LUMO energies (average = –3.54 eV), and

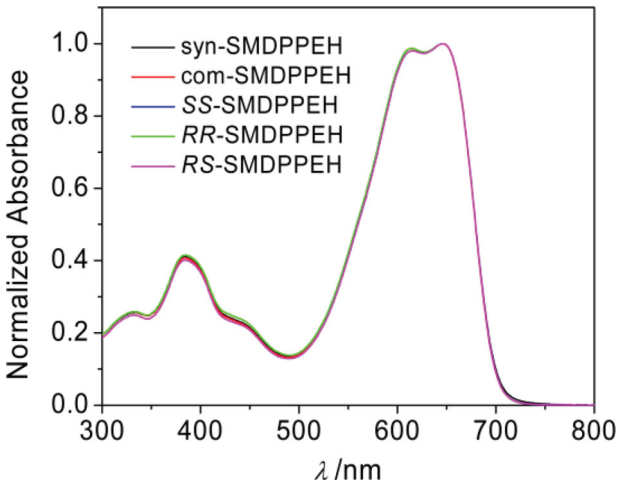

Figure 2. Normalized absorbance spectra of **SMDPPEH** in solution ($CHCl_3$; 20×10^{-6} M).

HOMO–LUMO gaps (average = 1.8 eV) estimated from the oxidation and reduction peak potentials are also consistent with the optical data.

2.4. Characterization of the SMDPPEH Compositions in the Solid State

The thermal properties of the **SMDPPEH** samples were studied by thermogravimetric analysis (TGA) and differential scanning calorimetry (DSC) in order to understand the effect of isomeric composition and EtHx stereochemistry on the bulk behavior of the materials. All compounds show similar thermal stability with loss of 5% of their original weight at high temperature (341–343 °C; Figure S20). DSC (**Table 2** and Figure S21) reveals a melting transition (T_m) of ~ 160 °C for four of the materials; this is increased significantly to 180 °C for the meso compound ***RS*-SMDPPEH**. An additional melting transition is found for the enantiomers ***RR*-** and ***SS*-SMDPPEH** (at 156 and 155 °C, respectively) implicating the co-existence of two different crystal phases. With the exception of ***RS*-SMDPPEH**, the materials all crystallize upon cooling (T_c) at ~ 130 °C. The higher T_c for the meso compound (154 °C), taken together with its higher T_m, speak to a greater crystallization tendency for this isomer formulation. This result is consistent with what was reported for ***RS*-DPP(TBFu)$_2$** that showed the highest thermal transition temperatures and lowest solubility among its independently studied isomers.[40] ***RS*-SMDPPEH** is accordingly also the least soluble of the **SMDPPEH** compositions in our hands.

Table 1. Optical properties of **SMDPPEH** in $CHCl_3$ (20×10^{-6} M).

Material	λ_{max} [nm]	λ_{onset} [nm]	$\varepsilon \times 10^4$ [$M^{-1} \cdot cm^{-1}$]	ΔE_{opt} [eV]
syn-SMDPPEH	385/616/646	700	6.2 ± 0.1	1.77
com-SMDPPEH	384/616/646	699	7.3 ± 0.2	1.77
SS-SMDPPEH	384/616/647	699	6.5 ± 0.2	1.77
RR-SMDPPEH	384/615/646	699	6.2 ± 0.1	1.77
RS-SMDPPEH	385/615/646	699	6.6 ± 0.1	1.77

Table 2. SMDPPEH thermal properties.

Material	5% Weight Loss [°C]	T_m [°C][a)]	T_c [°C][b)]
syn-SMDPPEH	342	158	*126*
com-SMDPPEH	341	159	*133*
SS-SMDPPEH	343	156/160	*132*[b]
RR-SMDPPEH	343	155/160	*127*[b]
RS-SMDPPEH	343	180	*154*

[a)]The 2nd and 3rd heating and cooling scan cycles were employed to determine the thermal transition temperatures, at a scan rate of 10 °C/min, under N_2 atmosphere; [b)]Although two crystallization peaks were expected for the enantiomers, they could not be resolved even upon changing the heating/cooling rate.

X-ray diffraction (XRD) was used to study the crystallinity of neat and blended (with PCBM) spin-coated **SMDPPEH** thin films prepared on silicon substrates (precoated with 25 nm thick PEDOT:PSS films to allow a direct comparison with films incorporated in photovoltaic devices, vide infra). For neat, unannealed films (**Figure 3**a) a single, relatively weak diffraction peak is observed for all five materials. The peaks for **syn-SMDPPEH** ($2\theta = 6.20°$; $d = 14.2$ Å), **com-SMDPPEH** ($2\theta = 6.16°$; $d = 14.3$ Å), and ***RS*-SMDPPEH** ($2\theta = 6.21°$; $d = 14.2$ Å) share similar 2θ values. Of these three the ***RS*-SMDPPEH** peak is most intense, consistent with the compound's intrinsically higher degree of crystallization (vide supra). Enantiomers ***SS*-SMDPPEH** ($2\theta = 6.66°$; $d = 13.3$ Å) and ***RR*-SMDPPEH** ($2\theta = 6.63°$; $d = 13.3$ Å) show expectedly nearly identical XRD spectra but a slightly tighter (by ~ 1 Å) molecular packing than the other three materials. After annealing (at 100 °C for 5 min), a 2–3 fold increase in diffraction intensity (and increase in degree of crystallization) is observed for all of the **SMDPPEH** materials (Figure 3b). **syn-SMDPPEH** and **com-SMDPPEH** continue to exhibit identical XRD spectra, with a single peak centered at $2\theta = 6.00°$ ($d = 14.7$ Å), indicating that the differences in isomer composition between these two compounds have little effect on neat film crystallinity. Neat, annealed films of ***SS*-SMDPPEH** and ***RR*-SMDPPEH** again show expectedly similar behavior, but now with two peaks ($2\theta = 5.54°$ ($d = 15.9$ Å) and $2\theta = 6.36°$ ($d = 13.9$ Å)) observed for each film. Implied are co-existing crystal phases, a result consistent with the DSC data (vide supra). The difference in relative intensity for the two peaks between the ***SS*-** and ***RR*-SMDPPEH** samples indicates a different fractional film coverage for the two phases, with both materials preferentially forming in the $d = 15.9$ Å phase while ***RR*-SMDPPEH** forms slightly more of the $d = 13.9$ Å phase. Precedent[79] leads one to suspect that such differences might arise from the clockwise substrate rotation during spin coating that was used here, which could affect the chiral materials differently. At any rate, it appears that even for enantiomers the film crystallinity can vary depending on subtle differences in film preparation. Interestingly, the ***RS*-SMDPPEH** XRD peak shifts about half an angstrom to a smaller d-spacing ($2\theta = 6.46°$; $d = 13.7$ Å) upon annealing, while the XRD peaks of the other four films shift toward slightly higher d-spacings. Again, the ***RS*-SMDPPEH** material shows the strongest peak

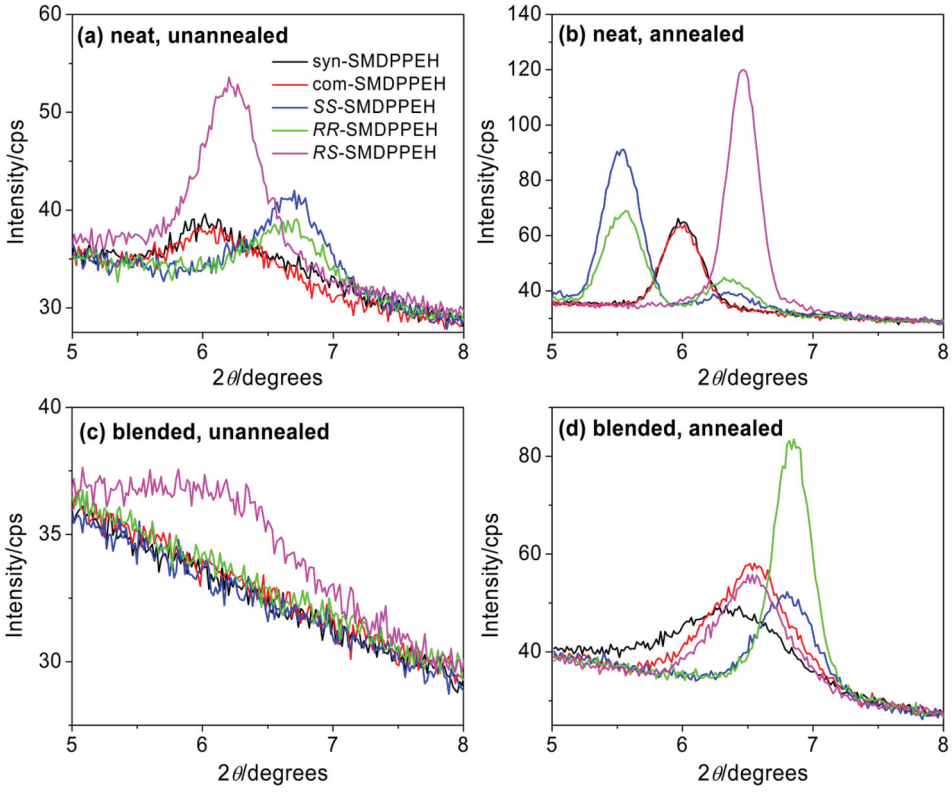

Figure 3. XRD spectra for spin-coated films of (a,b) neat **SMDPPEH** or (c,d) **SMDPPEH**:$PC_{61}BM$. Films (a,c) were not annealed, whereas films (b,d) were annealed at 100 °C for 5 minutes.

intensity, indicating a higher degree of crystallization in the film.

The full width at half maximum (FWHM) of the XRD peaks observed for neat films (Figures 3a,b) can be related to the size of the contributing crystallites using the Scherrer equation.[80] Crystallite sizes, calculated using this method, are observed to increase 2–3 fold for all five neat films after thermal annealing. Before thermal annealing, Scherrer grain sizes of 8, 9, 13, 11 and 15 nm (with a typical error of 2 nm) were found for **syn-**, **com-**, ***SS-***, ***RR-*** and ***RS-*****SMDPPEH**, respectively; after thermal annealing, the Scherrer grain sizes were increased to 25, 25, 27, 25 and 30 nm for **syn-**, **com-**, ***SS-***, ***RR-*** and ***RS-*****SMDPPEH**, respectively.

When blended in a 1:1 weight ratio with PCBM in solution, the spin coated films of **SMDPPEH** are completely amorphous with the notable exception of the ***RS-*****SMDPPEH**:PCBM film, which displays a weak, broad peak centered at $2\theta = 6.11°$ (d = 14.4 Å) (Figure 3c). The presence of PCBM along with rapid drying of the $CHCl_3$ solvent inhibits crystallization,[81,82] suggesting the effectiveness of the PCBM acceptor to frustrate the **SMDPPEH** molecular packing. Unlike the other four materials, crystallization of the ***RS-*****SMDPPEH**:PCBM film is not completely suppressed. However, after annealing at 100 °C for 5 minutes a single XRD peak is present for each material (Figure 3d). The peaks for **com-SMDPPEH** and ***RS-*****SMDPPEH** are both centered at $2\theta = 6.53°$ (d = 13.5 Å), while a broader peak is centered at $2\theta = 6.36°$ (d = 13.9 Å) for **syn-SMDPPEH**. The spectral differences here may be related to differences in isomer composition between the **syn-** and **com-SMDPPEH** materials. For ***SS-*** and ***RR-*****SMDPPEH**, a single peak for each is observed at $2\theta = 6.79°$ (d = 13.0 Å) and $2\theta = 6.84°$ (d = 12.9 Å), respectively. Again, we would expect identical behavior between the enantiomers, however small processing differences, for example the clockwise rotation of the spin coater, may contribute to the differences observed in peak intensity. Overall, the XRD patterns for these annealed blended films (Figure 3d) exhibit strong resemblance to those for the neat **SMDPPEH** films prior to annealing (Figure 3a), but are considerably different from those for the annealed neat films (Figure 3b). Comparing the annealed neat films to the annealed films blended with PCBM, it is clear that PCBM can have a strong effect on the phase adopted by the different **SMDPPEH** isomers. Of the five materials, the neat crystal structure appears to be maintained only by ***RS-*****SMDPEH** after blending with PCBM, while the other four materials show a significant shift toward shorter d-spacing upon PCBM addition. Again, Scherrer grain sizes were calculated from the FWHM of the blend film XRD peaks, with a size of 7 nm determined for the unannealed ***RS-*****SMDPPEH** film (no peaks were observed for the other materials under these conditions). After annealing, grain sizes of 8, 12, 17, 25 and 14 nm were found for **syn-**, **com-**, ***SS-***, ***RR-*** and ***RS-*****SMDPPEH**, respectively.

The thin film surface morphologies of the five **SMDPPEH** materials were investigated using atomic force microscopy (AFM). Neat, unannealed films (Figure S22) all show a random pattern of approximately 3 nm deep, 80–120 nm

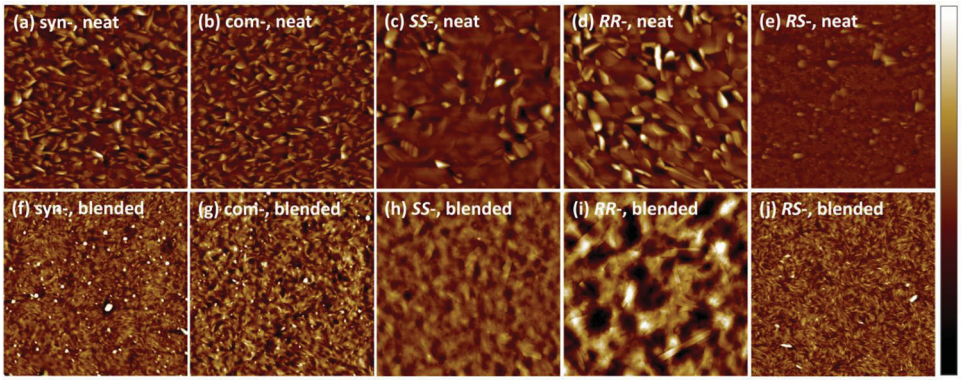

Figure 4. AFM images of spin-coated films of (a,f) **syn-SMDPPEH**, (b,g) **com-SMDPPEH**, (c,h) ***RS*-SMDPPEH**, (d,i) ***SS*-SMDPPEH** and (e,j) ***RR*-SMDPPEH**. All films were annealed at 100 °C for 5 minutes (for unannealed films see **Figure S22**). (a–e) are neat films while (f–j) are blended 1:1 by weight with PCBM. The full height scales (see the color bar shown at the far right of this figure) are 80 nm for (a–e), 10 nm for (f,g,j) and 40 nm for (h,i). The scanning area is 5 × 5 μm for all images.

wide indentations on an otherwise flat surface. The root-mean-square (RMS) roughness for all five films is in the range of 1.0–1.3 nm. Upon annealing, large crystal formation is observed (**Figures 4**a–e). The surfaces of the annealed neat films of **syn-SMDPPEH** and **com-SMDPPEH** (Figures 4a,b) appear nearly identical, covered with randomly oriented crystallites that are approximately 100–200 nm across and 20–40 nm tall. The annealed ***RR*-** and ***SS*-SMDPPEH** films (Figures 4d,e) both show noticeably larger domain features than the **syn-SMDPPEH** and **com-SMDPPEH** films, and contain a majority phase composed of flat, terrace structures with dimensions up to approximately 1 μm, as well as a minority phase composed of protruding crystals with sizes up to 500 nm. Based on the XRD patterns shown in Figure 3b, we assign the former to the d = 15.9 Å XRD peak and the latter to the d = 13.7 Å XRD peak. As indicated by the XRD peak intensities, the 13.7 Å phase is more prevalent on the ***RR*-SMDPPEH** surface (Figure 4e). The annealed neat film of ***RS*-SMDPPEH** (Figure 4c) is significantly flatter than the others, with an RMS roughness of 3.3 nm. The **syn-SMDPPEH**, **com-SMDPPEH**, ***SS*-SMDPPEH**, and ***RR*-SMDPPEH** films show RMS roughnesses of 9.3, 8.1, 6.6, and 10.0 nm, respectively.

Without any annealing, films blended with PCBM are quite flat and generally featureless, with RMS roughness of approximately 0.6 nm for all five materials (Figure S22). After annealing, however, two distinct morphologies are observed. For annealed **syn-SMDPPEH**:PCBM, **com-SMDPPEH**:PCBM, and ***RS*-SMDPPEH**:PCBM films (Figures 4f–h), aggregates protrude from the surface with heights of 5–20 nm and diameters of 30–150 nm (although there are fewer in the case of ***RS*-SMDPPEH**:PCBM). Randomly oriented crystallites are visible in the background. For annealed ***RR*-** and ***SS*-SMDPPEH**:PCBM films (Figures 4i,j), long, narrow crystallites decorate an undulating surface with peak-to-valley height of 30–40 nm. The annealed blended films were generally flatter than the annealed neat films, although less so for the ***RR*-** and ***SS*-** isomers, with RMS roughnesses of 1.3, 1.5, 3.3, 7.4 and 1.0 nm for annealed **syn-SMDPPEH**:PCBM, **com-SMDPPEH**:PCBM, ***SS*-SMDPPEH**:PCBM, ***RR*-SMDPPEH**:PCBM, and ***RS*-SMDPPEH**:PCBM films, respectively. In summary, very similar surface morphology is observed for unannealed films of all five isomers; however, upon thermal annealing significant differences are observed. The observed differences agree well with XRD data, and the techniques taken together suggest a number of different phases form depending on the isomer type and processing conditions.

Optical absorption spectra of **SMDPPEH** thin films prepared on glass substrates (precoated with 25 nm thick PEDOT:PSS films) are presented in **Figure 5**. All films show a peak at 420 nm that has been previously attributed to a π–π^* transition for both the thiophene and the central diketopyrrolopyrrole (DPP) units.[66] In the 500–900 nm wavelength region, intense absorptions are found that can be fit well with a set of three Gaussian peaks (see Figures S23 and S24; Table S2). The relative intensities and positions of the absorption peaks are related to crystal packing, as peaks arise from both intra- and intermolecular charge transfer. The apparent absorption at long wavelengths beyond the band gap for neat films of ***RS*-SMDPPEH** is attributed to light scattering. Given that neat unannealed films of **syn-SMDPPEH**, **com-SMDPPEH**, and ***RS*-SMDPPEH** show similar absorption spectra (Figure 5a) with peaks from Gaussian fitting centered at 610, 655, and 720 nm, they presumably share the same phase (with ***RS*-SMDPPEH** crystallizing to a greater degree). The results suggest that neat, unannealed films of **syn-SMDPPEH** and **com-SMDPPEH**—stereoisomeric mixtures—may be composed of the crystalline ***RS*-SMDPPEH** component with disordered regions containing the ***RR*-** and ***SS*-SMDPPEH** isomers in between. The conclusion is supported by the XRD data (Figure 3a). On the other hand, neat unannealed films of ***RR*-** and ***SS*-SMDPPEH** show slightly blue-shifted absorption peaks, with Gaussian fits centered at approximately 600, 650 and 720 nm, with the shoulder at 600 nm becoming more prominent. As seen in the XRD analysis above, these films crystallize into a different phase than the ***RS*-SMDPPEH** containing films.

After annealing, the spectral shape of the absorption from neat **syn-** and **com-SMDPPEH** films is relatively unchanged (Figure 5b), while a ~ 10 nm blue shift is observed for the longest wavelength peak from 720 nm to 710 nm. The ***RS*-SMDPPEH** absorption spectrum (Figure 5b), with peaks centered at 615, 660, and 730 nm (after annealing), no longer matches the absorption spectra of the isomeric mixtures,

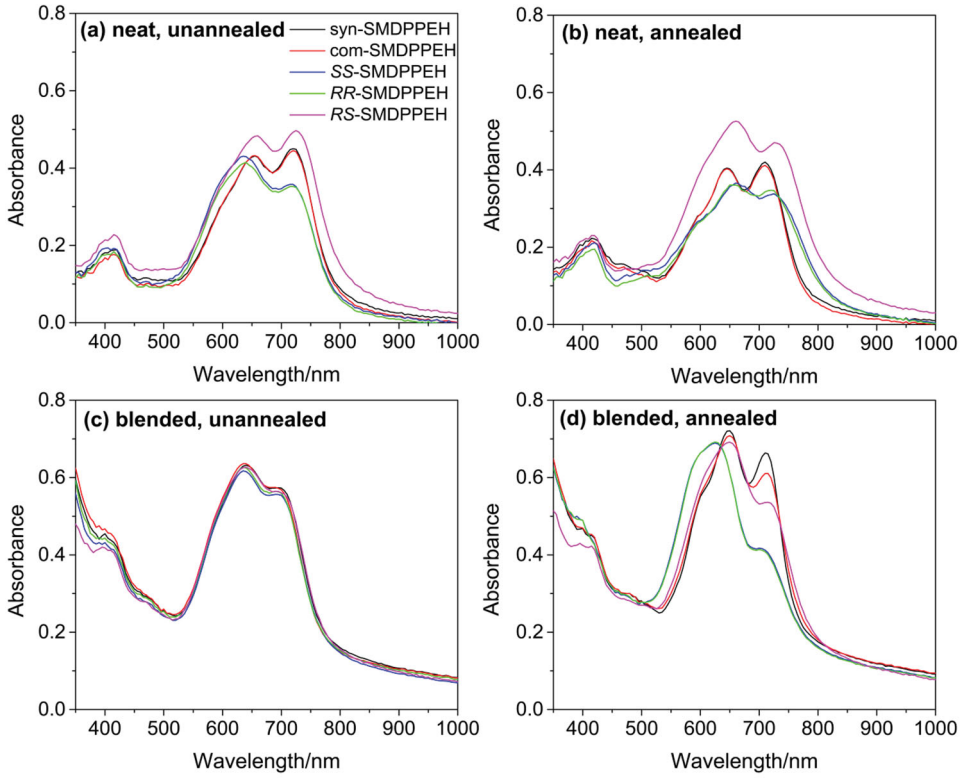

Figure 5. Absorption spectra for spin-coated films of **SMDPPEH** on glass/PEDOT:PSS. (a,c) were not annealed while (b,d) were annealed at 100 °C for 5 minutes. (a,b) are neat films while (c,d) are 1:1 by weight blends with PCBM.

suggesting that the meso compound adopts a different phase, in agreement with XRD measurements. Finally, after annealing, the ***SS*-SMDPPEH** and ***RR*-SMDPPEH** films also show nearly identical absorption spectra. Taking the neat film XRD and absorption data together, before annealing, the ***RS*-SMDPPEH** component of the isomer blends crystallizes the fastest, and thus dominates the absorption and XRD spectra of unannealed **syn-** and **com-SMDPPEH** films. However, after annealing, the isomer blends take on a crystal structure that is different from both the ***RR*-** and ***SS*- SMDPPEH** films on the one hand, and the ***RS*-SMDPPEH** film on the other. It can be concluded that after annealing the isomer blends crystallize into a structure that incorporates all three of the isomers.

The absorption spectra for unannealed **SMDPPEH**:PCBM blended films are nearly identical (Figure 5c) as a result of the low crystallinity of these films (for XRD, see Figure 3c). After annealing, however, all of the films are found to crystallize, resulting in differentiation of the absorption spectra (Figure 5d). The most pronounced change is observed for the annealed ***RR*-** and ***SS*-SMDPPEH**:PCBM films, for which the 600 nm peak becomes dominant, while the peak at 700 nm is strongly suppressed (see peak fitting in Figure S24). In agreement with the AFM and XRD results, the annealed ***RS*-SMDPPEH**:PCBM film absorption spectrum resembles that of the **syn-** and **com-SMDPPEH**:PCBM films, albeit with a reduction in intensity of the 700 nm peak. This peak has been previously assigned to intermolecular charge transfer in **syn-SMDPPEH** due to aggregate species,[66] and thus a reduction in its intensity may be interpreted as a reduction in crystallinity. However, such a conclusion is not supported by the AFM and XRD measurements in this work, which show that the surface morphology and degree of crystallization of annealed ***RS*-SMDPPEH**:PCBM, **syn-SMDPPEH**:PCBM, and **com-SMDPPEH**:PCBM films are quite similar.

2.5. Photovoltaic Device Performance

In order to probe the effect of side chain stereochemistry on the optoelectronic properties of the **SMDPPEH** materials, photovoltaic devices were fabricated with the structure: indium tin oxide (ITO)/PEDOT:PSS/**SMDPPEH**:PCBM/Al. Active layer formation was carried out in an identical fashion to the films analyzed above.

Unannealed devices showed very similar performance with the exception of the ***RS*-SMDPPEH**:PCBM device (**Table 3**, **Figure 6**a–c). For the other four materials, relatively low fill factors (FF) of 34–36% presumably result from fast recombination of charge carriers in the amorphous blends due to a lack of efficient charge extraction pathways. External quantum efficiencies (EQEs) in all four cases are also very similar (Figure 6c); as the light absorption efficiency was found to be the same, this suggests that the internal quantum efficiencies are nearly identical. The stereochemical purity of the 2-ethylhexyl side chains is not expected to significantly affect the electrical properties of the films when they are not allowed to crystallize. Thus, it is inferred that the more readily crystallizing ***RS*-SMDPPEH** material begins to phase segregate from the PCBM sans

Table 3. Characteristics for **SMDPPEH** photovoltaic devices.

Material	Annealed	V_{oc} [V]	J_{sc} [mA/cm^2]	FF [%]	PCE [%]
syn-SMDPPEH	no	0.742 ± 0.005	5.4 ± 0.2	35 ± 1	1.4 ± 0.1
com-SMDPPEH	no	0.742 ± 0.006	5.3 ± 0.2	34 ± 1	1.3 ± 0.1
SS-SMDPPEH	no	0.756 ± 0.005	5.5 ± 0.2	36 ± 1	1.5 ± 0.1
RR-SMDPPEH	no	0.752 ± 0.007	5.2 ± 0.4	35 ± 2	1.4 ± 0.2
RS-SMDPPEH	no	0.740 ± 0.005	6.5 ± 0.2	45 ± 2	2.2 ± 0.2
syn-SMDPPEH	yes	0.800 ± 0.005	7.3 ± 0.2	52 ± 1	3.0 ± 0.1
com-SMDPPEH	yes	0.766 ± 0.005	7.5 ± 0.3	50 ± 1	2.9 ± 0.1
SS-SMDPPEH	yes	0.705 ± 0.005	7.8 ± 0.3	52 ± 1	2.9 ± 0.1
RR-SMDPPEH	yes	0.703 ± 0.005	7.6 ± 0.3	50 ± 1	2.7 ± 0.1
RS-SMDPPEH	yes	0.688 ± 0.005	5.1 ± 0.2	55 ± 1	1.9 ± 0.1

annealing, leading to enhanced charge extraction in the corresponding device and a significantly higher FF of 45%.

For annealed devices (Figures 6d–f and Table 3) the performance is again quite similar for all of the devices except those featuring ***RS*-SMDPPEH**. The most dramatic change after annealing for the other four materials is the increase in FF to 50–52%, a 45% relative increase compared to the unannealed cases. Additionally, peak EQE increases from 30% for the unannealed devices up to 43–45% for the annealed devices, resulting in a relative increase in J_{SC} by 35–45%. Clearly, the crystallization that occurs during the annealing step for the **syn-SMDPPEH**:PCBM, **com-SMDPPEH**:PCBM, ***SS*-SMDPPEH**:PCBM, and ***RR*-SMDPPEH**:PCBM devices results in an improved photocurrent generation efficiency. For these annealed devices, the EQE spectral shape matches the film absorption spectra above, with ***RR*-** and ***SS*-SMDPPEH** showing stronger absorption from the 600 nm peak and **syn-** and **com-SMDPPEH** showing stronger absorption from the 700 nm peak. On balance, the spectral shift results in a similar short-circuit current (J_{SC}) of 7.3–7.8 mA/cm^2 for these four annealed devices. Differences in device performance for ***RR*-** and ***SS*-SMDPPEH** may be related to differences in the degree of donor crystallization, as observed in the XRD data. A significant reduction in open-circuit voltage (V_{OC}) is observed for the ***RR*-** and ***SS*-SMDPPEH** devices (0.703 V and 0.705 V, respectively) relative to the **syn-** and **com-SMDPPEH**

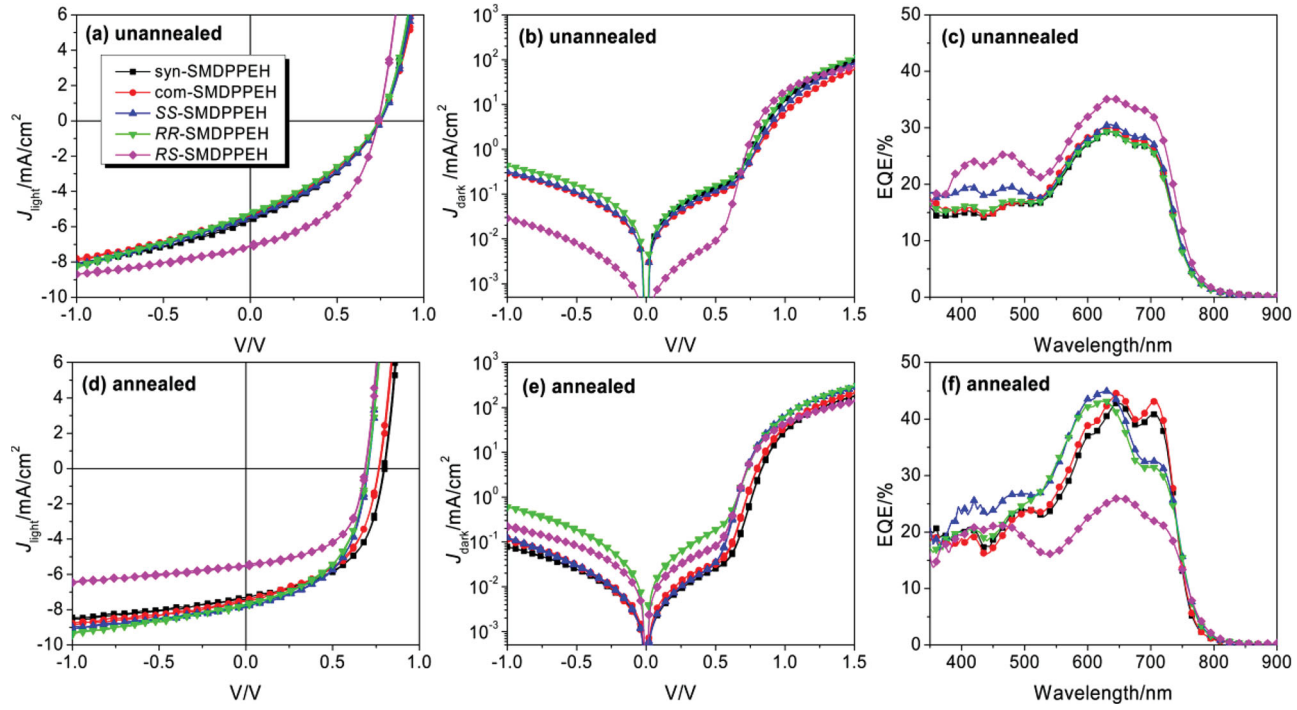

Figure 6. Characterization of **SMDPPEH** bulk heterojunction photovoltaic devices. (a,d) show current density under 1 sun AM1.5G illumination, (b,e) show dark current density, and (c,f) are EQE spectra. (a–c) were not annealed, while (d–f) were annealed at 100 °C for 5 minutes.

devices (0.800 V and 0.766 V, respectively). If these differences in V_{OC} resulted from a change in band gap (E_g), we would expect to see a red shift of 30–50 nm in the absorption onset of the ***RR*-** and ***SS*-SMDPPEH** devices relative to the **syn-** and **com-SMDPPEH** devices. A red shift is indeed observed in the onset of EQE, but only by approximately 5–10 nm. However, the dark current in Figure 6e can fully account for the difference in V_{OC} between the devices, specifically due to the difference in diode reverse-bias saturation current density, which was found to be 1.8×10^{-7} mA/cm^2 for the ***RR*-**, ***SS*-**, and ***RS*-SMDPPEH** devices, and 4.4×10^{-8} and 1.9×10^{-8} mA/cm^2 for the **syn-** and **com-SMDPPEH** devices, respectively (see fitting results in Figure S25). The discrepancy may arise from a difference in the relative shift of the optical and transport gaps.[83]

Unlike the other four devices, annealing of the ***RS*-SMDPPEH**:PCBM device results in a reduction in EQE, and therefore a reduction in J_{SC}. Differences in overall absorption cannot explain the reduction in EQE observed here, as peak EQE for the ***RS*-SMDPPEH**:PCBM device is only 26% (Figure 6f). Instead, some internal element of photocurrent generation efficiency must be negatively affected by the annealed ***RS*-SMDPPEH**:PCBM film's morphology.

Hole-only devices with the structure ITO/PEDOT:PSS/**SMDPPEH**:PCBM/MoO_x/Au were fabricated in order to investigate charge transport in these materials (Figures S26 and S27). A transition from Ohmic to space-charge-limited current (SCLC) was observed at approximately 0.5 V for all of the **SMDPPEH** compositions. The SCLC region of each current-voltage curve was fit according to Child's law to determine the hole mobility.[84] Values of 1.1×10^{-5}, 6.9×10^{-6}, 2.0×10^{-5}, 9.6×10^{-6}, and 1.7×10^{-5} cm^2/V·s were found for unannealed films of **syn-SMDPPEH**:PCBM, **com-SMDPPEH**:PCBM, ***SS*-SMDPPEH**:PCBM, ***RR*-SMDPPEH**:PCBM, and ***RS*-SMDPPEH**:PCBM, respectively. Upon thermal annealing, the hole mobility of all five of the films increased by approximately half to one full order of magnitude, with values of 4.8×10^{-5}, 6.8×10^{-5}, 9.1×10^{-5}, 8.3×10^{-5}, and 6.9×10^{-5} cm^2/V·s for **syn-SMDPPEH**:PCBM, **com-SMDPPEH**:PCBM, ***SS*-SMDPPEH**:PCBM, ***RR*-SMDPPEH**:PCBM, and ***RS*-SMDPPEH**:PCBM, respectively.

Overall, we find that the photovoltaic device performance is only weakly affected by the differences in morphology between the pure stereoisomers ***SS*-/*RR*-SMDPPEH** and the stereoisomeric mixtures **syn-/com-SMDPPEH**. Shifted absorption spectra balance out to give approximately the same coverage of the solar spectrum. Moreover, although very different surface morphologies are observed with AFM, coincidently the ability of each of these materials to transport charges is only weakly affected. However, the ***RS*-SMDPPEH** devices perform much differently from those made with the other four materials. This isomer crystallizes more rapidly, resulting in differences in optimum film processing. Most notably, while the PCE of the other devices improved upon mild thermal annealing at 100 °C, the performance of the ***RS*-SMDPPEH**:PCBM device deteriorated with the same treatment. It is expected that a more thorough optimization of processing conditions for this material could bring the overall efficiency closer to that of the other four materials.

3. Conclusions

The goal of the current work has been to evaluate the consequences of 2-ethylhexyl solubilizing group chirality, and the isomeric complexity it creates, on small π-conjugated molecule morphology and bulk heterojunction photovoltaic device performance. To this end, **SMDPPEH**, a commercially-available organic semiconductor, was prepared in isomerically defined form from enantiomerically pure reagents. The crystallization behavior and optoelectronic properties—neat and as blends with PCBM—of the three pure isomers (***RR*-**, ***SS*-**, and ***RS*-SMDPPEH**) were systematically compared to typical ~ 1:1:2 isomer mixtures purchased commercially (**com-SMDPPEH**) or prepared in the laboratory (**syn-SMDPPEH**).

Expectedly and gratifyingly, the enantiomers (***RR*-** and ***SS*-SMDPPEH**) showed overall similar thin film morphology and absorption (neat and as blends; annealed or unannealed), and consequently bulk heterojunction device performance throughout the studies. Although different in these respects from the enantiomers, and despite small differences in isomer composition, **syn-** and **com-SMDPPEH** showed similar morphologies and optoelectronic characteristics. All four **SMDPPEH** compositions were amorphous as 1:1 blends with PCBM without post-deposition thermal annealing, a situation where the crystallinity, and therefore stereochemical information, was lost. ***RS*-SMDPPEH** was found to crystallize most readily of the pure isomers, in the presence and absence of PCBM, and consequently dominated the absorption and XRD profiles of the neat isomeric mixtures. Indeed, ***RS*-SMDPPEH** maintained some crystallinity in the presence of PCBM prior to thermal annealing resulting in a 50–60% improvement in photovoltaic device performance relative to the other four compositions.

After thermal annealing, ***RR*/*SS*-SMDPPEH**, **syn/com-SMDPPEH**, and ***RS*-SMDPPEH** revealed different crystal structures and morphologies suggesting that the isomer mixtures (**syn-** and **com-SMDPPEH**) adopted a phase that incorporated all three components. Blending with PCBM had a strong effect on the crystal packing (by XRD), where again the more strongly crystallizing ***RS*-SMDPPEH** dominated the profiles of the isomer mixtures. For **syn-**, **com-**, ***SS*-**, and ***RR*-SMDPPEH**, a substantial increase in photovoltaic device performance was observed after thermal annealing, while ***RS*-SMDPPEH** showed a decrease in device performance. Overall, the stereocenter affected the morphology of the active layer and the thin film absorption spectra, but had a relatively weak effect on the overall photovoltaic performance.

The extent to which alkyl side chain stereochemistry should be considered an important tunable parameter in materials design is most certainly device/application dependent. To wit, Nguyen and coworkers demonstrated that while the isolated stereoisomers of **DPP(TBFu)$_2$** showed similar morphologies, ***RS*-DPP(TBFu)$_2$** displayed much higher FET mobility (before and after annealing) as a consequence of its crystal structure with tighter π–π stacking, as well as a more homogenous domain shape/size and smaller film roughness (versus ***RR*-** and ***SS*-DPP(TBFu)$_2$**). The study conveys the importance of isomeric composition/purity on a small molecule's carrier mobility, and the observation appears generally extendable to other

π-conjugated systems.[40] Our work shows that the side chain chirality, while strongly impacting the thin film morphology and optical properties of **SMDPPEH**, has modest effects on the photovoltaic performance of the material as blends with PCBM. While this does not mean that side chain stereochemistry does not influence blend structure, it does suggest that the structural consequences lead to fortuitously compensatory optoelectronic effects in this context. Studies among additional classes of semiconductors will expose whether side chain chirality can be employed to rationally improve OPV efficiency or whether it can be safely "ignored".

4. Experimental Section

General Synthetic Methods and Molecular Characterization: Reagents and solvents were purchased from commercial sources and used without further purification unless otherwise specified. THF, Et_2O, CH_2Cl_2, and DMF were degassed in 20 L drums and passed through two sequential purification columns (activated alumina; molecular sieves for DMF) under a positive argon atmosphere. 2-(5′-Hexyl-[2,2′-bithiophen]-5-yl)-4,4,5,5-tetramethyl-1,3,2-dioxaborolane and [1,1′-bis(diphenylphosphino)ferrocene]dichloro palladium(II) (complex with dichloromethane, $[Pd(dppf)Cl_2{\cdot}CH_2Cl_2]$) were purchased from Sigma-Aldrich and used as received. Thin layer chromatography (TLC) was performed on SiO_2-60 F_{254} aluminum plates with visualization by UV light or staining. Flash column chromatography was performed using Silica gel technical grade, pore size 60 Å, 230–400 mesh particle size, 40–63 μm particle size from Sigma-Aldrich. Specific Optical rotations were obtained on a JASCO P-2000 Series Polarimeter (wavelength = 589 nm) and then corresponded to the literature. 500 (125) MHz ^{1}H (^{13}C) NMR were recorded on an INOVA 500 spectrometer. Chemical shifts (δ) are given in parts per million (ppm) relative to TMS and referenced to residual protonated solvent purchased from Cambridge Isotope Laboratories, Inc. ($CDCl_3$: δ_H 7.26 ppm, δ_C 77.16 ppm; DMSO-d_6: δ_H 2.50 ppm, δ_C 39.52 ppm). Abbreviations used are s (singlet), d (doublet), t (triplet), q (quartet), quin (quintet), hp (heptet), b (broad), and m (multiplet). ESI-TOF-, APCI-TOF-, and DART-TOF-MS spectra were recorded on an Agilent 6210 TOF spectrometer with MassHunter software. EI-MS (70 eV) spectra were recorded on a Thermo Scientific DSQ MS after sample introduction via GC with data processing on Xcalibur software (accurate masses are calculated with the CernoBioscience MassWorks software). MALDI-TOF-MS was performed on a AB Sciex TOF/TOF 5800 in reflectron mode while the data is processed with Data Explorer. Samples were prepared by mixing the molecule of interest in dithranol (DTL) and then applied onto the MALDI plate. Isomeric purity was determined by chiral HPLC analysis (Shimadzu) using a Chiralpack IA column (8% *i*-PrOH in hexanes, 0.8 mL/min, 350 nm).

Thermal Analysis: Thermal gravimetric analysis (TGA) was performed using a TA Instruments TGA Q5000–0121 V3.8 Build 256 at a heating rate of 10 °C/min using 1–3 mg of sample in a 100 μL platinum pan (under nitrogen). The data was analyzed on Universal Analysis 2000 4.4A software. Differential Scanning Calorimetry (DSC) was performed using a TA Instruments DSC Q1000–0620 V9.9 at a heating/cooling rate of 10 °C/min using 1–3 mg of sample in a sealed aluminum pan, with respect to an empty aluminum reference pan. Three cycles of heating and subsequent cooling were performed. The data was analyzed on Universal Analysis 2000 4.4A software.

Solution Absorption Measurements: Absorption spectra were measured for at least six different concentrations (2.5–30 μM) of **SMDPPEH** using a Cary 100 Bio spectrophotometer and 1 cm quartz cuvettes. All solvents were spectrophotometric grade and purchased from Sigma-Aldrich. The absorption intensity at λ_{max} was then plotted against the concentration in all cases to confirm, by linearity, that the compounds followed Beer's law. Molar extinction coefficients (ε) were determined from the linear plot for each compound (where $A = \varepsilon bc$).

Thin Film Characterization: UV-vis absorption (thin film) measurements were carried out with a calibrated Newport 818-UV Si photodiode illuminated by a Newport Oriel Apex illuminator and monochromator system chopped at 400 Hz. The signal was detected using a Stanford Research Systems SR830-DSP lock-in amplifier. Atomic force microscopy was carried out using a Veeco Innova AFM in tapping mode with a silicon tip (radius ~ 8 nm) at 325 kHz with a force constant of approximately 40 N/m. X-ray diffraction measurements were performed using a PANalytical X'Pert Powder diffractometer operated in the θ-2θ mode using Cu Kα radiation ($\lambda = 1.54$ Å).

Device Fabrication and Characterization: Organic photovoltaic devices were fabricated on commercial indium-tin oxide (ITO) coated glass substrates with a sheet resistance of ~15 Ω/square, while films for XRD and AFM analysis were fabricated on Si(100) substrates. The substrates were sequentially sonicated for 15 minutes in detergent, water, acetone and isopropanol before UV-ozone treatment for an additional 15 minutes. PEDOT:PSS (Clevios AI4083) was spin-coated in air at 8000 rpm to form a ~25 nm thick layer, which was annealed at 150 °C for 30 minutes in air before passing into a nitrogen glovebox (H_2O ~ 1 ppm). Photovoltaic active layers were spin-coated from a 5:5 mg/mL solution of **SMDPPEH**:$PC_{61}BM$ in $CHCl_3$ at 500 rpm to form a ~110 nm thick layer. Films were then passed into a vacuum chamber pumped down to 10^{-6} Torr, and a 100 nm Al cathode was evaporated through a shadow mask with thicknesses monitored by a quartz crystal monitor. The cross-bar geometry was used to define an active area of 4 mm^2 for the organic photovoltaic cells. After aluminum deposition, some devices were annealed at 100 °C for 5 minutes in a nitrogen glovebox, and then encapsulated with a UV-curable epoxy layer to prevent degradation from exposure to ambient oxygen and water before characterization in air.

Devices were characterized under illumination from a 150W Xe-arc lamp solar simulator with a KG1 filter, calibrated to 1 sun intensity using the AM1.5G spectrum. External quantum efficiency measurements were carried out with a calibrated Newport 818-UV Si photodiode illuminated by a Newport Oriel Apex illuminator and monochromator system chopped at 400 Hz. The photocurrent signal was detected using a Stanford Research Systems SR830-DSP lock-in amplifier.

Supporting Information

Supporting Information is available from the Wiley Online Library or from the author.

Acknowledgements

R. K. C. acknowledges financial support from the National Science Foundation (CHE-1057411). J.X. and R.K.C. also acknowledge partial financial support from the Research Corporation for Science Advancement (Scialog Award 20316) and the University of Florida Office of Research.

Received: March 31, 2014
Revised: May 19, 2014
Published online: July 22, 2014

[1] B. Walker, C. Kim, T.-Q. Nguyen, *Chem. Mater.* **2011**, *23*, 470.
[2] M. A. Naik, N. Venkatramaiah, C. Kanimozhi, S. Patil, *J. Phys. Chem. C* **2012**, *116*, 26128.
[3] T. Lei, J. Wang, J. Pei, *Chem. Mater.* **2014**, *26*, 594.
[4] J. H. Seo, *Synth. Met.* **2012**, *162*, 748.
[5] S. Subramaniyan, H. Xin, F. S. Kim, S. Shoaee, J. R. Durrant, S. A. Jenekhe, *Adv. Energy Mater.* **2011**, *1*, 854.

[6] Z. B. Henson, P. Zalar, X. Chen, G. C. Welch, T.-Q. Nguyen, G. C. Bazan, *J. Mater. Chem. A* **2013**, *1*, 11117.
[7] Z. Zhang, S. Zhang, J. Min, C. Cui, H. Geng, Z. Shuai, Y. Li, *Macromolecules* **2012**, *45*, 2312.
[8] L. Fang, Y. Zhou, Y.-X. Yao, Y. Diao, W.-Y. Lee, A. L. Appleton, R. Allen, J. Reinspach, S. C. B. Mannsfeld, Z. Bao, *Chem. Mater.* **2013**, *25*, 4874.
[9] O. Kwon, J. Jo, B. Walker, G. C. Bazan, J. H. Seo, *J. Mater. Chem. A* **2013**, *1*, 7118.
[10] R. Kroon, A. Lundin, C. Lindqvist, P. Henriksson, T. T. Steckler, M. R. Andersson, *Polymer* **2013**, *54*, 1285.
[11] A. Tang, Z. Lu, S. Bai, J. Huang, Y. Chen, Q. Shi, C. Zhan, J. Yao, *Chem. Asian J.* **2014**, *9*, 883.
[12] J. Kesters, S. Kudret, S. Bertho, N. Van den Brande, M. Defour, B. Van Mele, H. Penxten, L. Lutsen, J. Manca, D. Vanderzande, W. Maes, *Org. Electr.* **2014**, *15*, 549.
[13] S. Ota, S. Minami, K. Hirano, T. Satoh, Y. Ie, S. Seki, Y. Aso, M. Miura, *RSC Adv.* **2013**, *3*, 12356.
[14] Y. Li, Y. Chen, X. Liu, Z. Wang, X. Yang, Y. Tu, X. Zhu, *Macromolecules* **2011**, *44*, 6370.
[15] J. Min, Y. N. Luponosov, A. Gerl, M. S. Polinskaya, S. M. Peregudova, P. V. Dmitryakov, A. V. Bakirov, M. a. Shcherbina, S. N. Chvalun, S. Grigorian, N. Kaush-Busies, S. a. Ponomarenko, T. Ameri, C. J. Brabec, *Adv. Energy Mater.* **2014**, *4*, 1301234.
[16] R. Fitzner, C. Elschner, M. Weil, C. Uhrich, C. Körner, M. Riede, K. Leo, M. Pfeiffer, E. Reinold, E. Mena-Osteritz, P. Bäuerle, *Adv. Mater.* **2012**, *24*, 675.
[17] A. El Labban, J. A. Bartelt, J. D. Douglas, W. R. Mateker, J. M. J. Fre, M. D. Mcgehee, P. M. Beaujuge, *J. Am. Chem. Soc.* **2013**, *135*, 4656.
[18] A. Casey, R. S. Ashraf, Z. Fei, M. Heeney, *Macromolecules* **2014**, *47*, 2279.
[19] A. D. Hendsbee, J.-P. Sun, L. R. Rutledge, I. G. Hill, G. C. Welch, *J. Mater. Chem. A* **2014**, *2*, 4198.
[20] B. Wang, J. Zhang, H. L. Tam, B. Wu, W. Zhang, M. S. Chan, F. Pan, G. Yu, F. Zhu, M. S. Wong, *Polym. Chem.* **2014**, *5*, 836.
[21] H. Zhong, Z. Li, E. Buchaca-Domingo, S. Rossbauer, S. E. Watkins, N. Stingelin, T. D. Anthopoulos, M. Heeney, *J. Mater. Chem. A* **2013**, *1*, 14973.
[22] B. Fu, J. Baltazar, A. R. Sankar, P.-H. Chu, S. Zhang, D. M. Collard, E. Reichmanis, *Adv. Funct. Mater.* **2014**, *24*, 3734.
[23] D. Baran, A. Balan, T. Stubhan, T. Ameri, L. Toppare, C. J. Brabec, *Synth. Met.* **2012**, *162*, 2047.
[24] I. Osaka, M. Saito, T. Koganezawa, K. Takimiya, *Adv. Mater.* **2014**, *26*, 331.
[25] K. H. Hendriks, W. Li, M. M. Wienk, R. A. J. Janssen, *Adv. Energy Mater.* **2013**, *3*, 674.
[26] P. Shen, H. Bin, X. Chen, Y. Li, *Org. Electr.* **2013**, *14*, 3152.
[27] C.-H. Cho, H. J. Kim, H. Kang, T. J. Shin, B. J. Kim, *J. Mater. Chem.* **2012**, *22*, 14236.
[28] H.-S. Chung, W.-H. Lee, C. E. Song, Y. Shin, J. Kim, S. K. Lee, W. S. Shin, S.-J. Moon, I.-N. Kang, *Macromolecules* **2014**, *47*, 97.
[29] Y. Li, J. Zou, H. Yip, C. Li, Y. Zhang, C. Chueh, J. Intemann, Y. Xu, P. Liang, Y. Chen, A. K. Jen, *Macromolecules* **2013**, *46*, 5497.
[30] T. Lei, J.-Y. Wang, J. Pei, *Acc. Chem. Res.* **2014**, *47*, 1117.
[31] T. Harschneck, N. Zhou, E. F. Manley, S. J. Lou, X. Yu, M. R. Butler, A. Timalsina, R. Turrisi, M. A. Ratner, L. X. Chen, R. P. H. Chang, A. Facchetti, T. J. Marks, *Chem. Commun.* **2014**, *50*, 4099.
[32] T. Nakanishi, Y. Shirai, T. Yasuda, L. Han, *J. Polym. Sci. Part A Polym. Chem.* **2012**, *50*, 4829.
[33] I. Meager, R. S. Ashraf, S. Mollinger, B. C. Schroeder, H. Bronstein, D. Beatrup, M. S. Vezie, T. Kirchartz, A. Salleo, J. Nelson, I. McCulloch, *J. Am. Chem. Soc.* **2013**, *135*, 11537.
[34] J. W. Rumer, C. K. L. Hor, I. Meager, C. P. Yau, Z. Huang, C. B. Nielsen, S. E. Watkins, H. Bronstein, I. McCulloch, *J. Org. Semicond.* **2013**, *1*, 30.
[35] V. S. Gevaerts, E. M. Herzig, M. Kirkus, K. H. Hendriks, M. M. Wienk, J. Perlich, P. Mu, R. A. J. Janssen, *Chem. Mater.* **2014**, *26*, 916.
[36] J. Kumagai, K. Hirano, T. Satoh, S. Seki, M. Miura, *J. Phys. Chem. B* **2011**, *115*, 8446.
[37] R. Fitzner, E. Mena-Osteritz, A. Mishra, G. Schulz, E. Reinold, M. Weil, C. Körner, H. Ziehlke, C. Elschner, K. Leo, M. Riede, M. Pfeiffer, C. Uhrich, P. Bäuerle, *J. Am. Chem. Soc.* **2012**, *134*, 11064.
[38] T. Yasuda, Y. Shinohara, T. Matsuda, L. Han, T. Ishi-i, *J. Polym. Sci., Part A Polym. Chem* **2013**, *51*, 2536.
[39] Q. Wu, S. Ren, M. Wang, X. Qiao, H. Li, X. Gao, X. Yang, D. Zhu, *Adv. Funct. Mater.* **2013**, *23*, 2277.
[40] J. Liu, Y. Zhang, H. Phan, A. Sharenko, P. Moonsin, B. Walker, V. Promarak, T.-Q. Nguyen, *Adv. Mater.* **2013**, *25*, 3645.
[41] C. R. G. Grenier, S. J. George, T. J. Joncheray, E. W. Meijer, J. R. Reynolds, *J. Am. Chem. Soc.* **2007**, *129*, 10694.
[42] G. C. Bazan,L. Ying, P. Zalar, T.-Q. Nguyen,US Patent 8 729 221 B2 **2014**.
[43] M. Verswyvel, F. Monnaie, G. Koeckelberghs, *Macromolecules* **2011**, *44*, 9489.
[44] Y. S. Jeong, K. Akagi, *Macromolecules* **2011**, *44*, 2418.
[45] K. Van den Bergh, I. Cosemans, T. Verbiest, G. Koeckelberghs, *Macromolecules* **2010**, *43*, 3794.
[46] Y. Zheng, J. Cui, J. Zheng, X. Wan, *J. Mater. Chem.* **2010**, *20*, 5915.
[47] L. A. P. Kane-Maguire, G. G. Wallace, *Chem. Soc. Rev.* **2010**, *39*, 2545.
[48] E. Yashima, K. Maeda, H. Iida, Y. Furusho, K. Nagai, *Chem. Rev.* **2009**, *109*, 6102.
[49] W. Vanormelingen, K. Van Den Bergh, T. Verbiest, G. Koeckelberghs, *Macromolecules* **2008**, *4*, 5582.
[50] T. Lei, J.-Y. Wang, J. Pei, *Chem. Mater.* **2014**, *26*, 594.
[51] J. Mei, Z. Bao, *Chem. Mater.* **2014**, *26*, 604.
[52] L. Yang, H. Zhou, W. You, C. Hill, N. Carolina, *J. Phys. Chem. C* **2010**, *114*, 16793.
[53] O. P. Lee, A. T. Yiu, P. M. Beaujuge, C. H. Woo, T. W. Holcombe, J. E. Millstone, J. D. Douglas, M. S. Chen, J. M. J. Fréchet, *Adv. Mater.* **2011**, *23*, 5359.
[54] T. W. Holcombe, J.-H. Yum, J. Yoon, P. Gao, M. Marszalek, D. Di Censo, K. Rakstys, M. K. Nazeeruddin, M. Graetzel, *Chem. Commun.* **2012**, *48*, 10724.
[55] A. B. Tamayo, X.-D. Dang, B. Walker, J. Seo, T. Kent, T.-Q. Nguyen, *Appl. Phys. Lett.* **2009**, *94*, 103301.
[56] D. H. Lee, M. J. Lee, H. M. Song, B. J. Song, K. D. Seo, M. Pastore, C. Anselmi, S. Fantacci, F. De Angelis, M. K. Nazeeruddin, M. Gräetzel, H. K. Kim, *Dyes Pigments* **2011**, *91*, 192.
[57] S. Loser, C. J. Bruns, H. Miyauchi, R. P. Ortiz, A. Facchetti, S. I. Stupp, T. J. Marks, *J. Am. Chem. Soc.* **2011**, *133*, 8142.
[58] G. C. Welch, L. a. Perez, C. V. Hoven, Y. Zhang, X.-D. Dang, A. Sharenko, M. F. Toney, E. J. Kramer, T.-Q. Nguyen, G. C. Bazan, *J. Mater. Chem.* **2011**, *21*, 12700.
[59] D. Sahu, C.-H. Tsai, H.-Y. Wei, K.-C. Ho, F.-C. Chang, C.-W. Chu, *J. Mater. Chem.* **2012**, *22*, 7945.
[60] Y. Sun, G. C. Welch, W. L. Leong, C. J. Takacs, G. C. Bazan, A. J. Heeger, *Nat. Mater.* **2012**, *11*, 44.
[61] J. Mei, K. R. Graham, R. Stalder, J. R. Reynolds, *Org. Lett.* **2010**, *12*, 660.
[62] J. K. Park, C. Kim, B. Walker, T.-Q. Nguyen, J. H. Seo, *RSC Adv.* **2012**, *2*, 2232.
[63] G. Zhang, Y. Fu, Z. Xie, Q. Zhang, *Macromolecules* **2011**, *44*, 1414.
[64] M. Oda, H.-G. Nothofer, U. Scherf, V. Šunjić, D. Richter, W. Regenstein, D. Neher, *Macromolecules* **2002**, *35*, 6792.
[65] T. Akaba, K. Yonezawa, H. Kamioka, T. Yasuda, L. Han, Y. Moritomo, *Appl. Phys. Lett.* **2013**, *102*, 133901.
[66] A. Tamayo, T. Kent, M. Tantitiwat, M. a. Dante, J. Rogers, T.-Q. Nguyen, *Energy Environ. Sci.* **2009**, *2*, 1180.

[67] S. Gemma, E. Gabellieri, S. Sanna Coccone, F. Martí, O. Taglialatela-Scafati, E. Novellino, G. Campiani, S. Butini, *J. Org. Chem.* **2010**, *75*, 2333.
[68] D. A. Evans, T. L. Shih, *J. Am. Chem. Soc.* **1981**, 2127.
[69] C. Aquino, M. Sarkar, M. J. Chalmers, K. Mendes, T. Kodadek, G. C. Micalizio, *Nat. Chem.* **2012**, *4*, 99.
[70] D. M. Hodgson, N. S. Kaka, *Angew. Chem. Int . Ed.* **2008**, *47*, 9958.
[71] B. Tylleman, G. Gbabode, C. Amato, C. Buess-Herman, V. Lemaur, J. Cornil, R. Gómez Aspe, Y. H. Geerts, S. Sergeyev, *Chem. Mater.* **2009**, *21*, 2789.
[72] F. He, W. Wang, W. Chen, T. Xu, S. B. Darling, J. Strzalka, Y. Liu, L. Yu, *J. Am. Chem. Soc.* **2011**, *133*, 3284.
[73] B. S. Souza, E. C. Leopoldino, D. W. Tondo, J. Dupont, F. Nome, *Langmuir* **2012**, *28*, 833.
[74] H. Tamagawa, H. Takikawa, K. Mori, *Eur. J. Org. Chem.* **1999**, 973.
[75] A. B. Tamayo, M. Tantiwiwat, B. Walker, T.-Q. Nguyen, *J. Phys. Chem. C* **2008**, *112*, 15543.
[76] J. R. Matthews, W. Niu, A. Tandia, A. L. Wallace, J. Hu, W.-Y. Lee, G. Giri, S. C. B. Mannsfeld, Y. Xie, S. Cai, H. H. Fong, Z. Bao, M. He, *Chem. Mater.* **2013**, *25*, 782.
[77] M. E. Farahat, H.-Y. Wei, M. A. Ibrahem, K. M. Boopathi, K.-H. Wei, C.-W. Chu, *RSC Adv.* **2014**, *4*, 9401.
[78] T.-Q. Nguyen, A. B. Tamayo, B. Walker, T. Kent, C. Kim, M. Tantiwiwat, US Patent 2010/0326525 A1 **2010**.
[79] T. Yamaguchi, T. Kimura, H. Matsuda, T. Aida, *Angew. Chem.* **2004**, *116*, 6510.
[80] P. S. Determination, *Phys. Rev.* **1939**, *56*, 978.
[81] G. Li, Y. Yao, H. Yang, V. Shrotriya, G. Yang, Y. Yang, *Adv. Funct. Mater.* **2007**, *17*, 1636.
[82] H. Lu, B. Akgun, T. P. Russell, *Adv. Funct. Mater.* **2011**, *1*, 870.
[83] S. Braun, W. R. Salaneck, M. Fahlman, *Adv. Mater.* **2009**, *21*, 1450.
[84] A. Rose, *Phys. Rev.* **1955**, *97*, 1538.